Part One

Fundamentals

1

Overview of Magnetic Nanomaterials

Ziyu Yang,[1] Shuang Qiao,[1] Shouheng Sun,[2] and Yanglong Hou[1]

[1]*Peking University, College of Engineering, Department of Materials Science and Engineering, 5 Yi He Yuan Road, Beijing 100871, China*
[2]*Brown University, Department of Chemistry, 324 Brook Street, Providence, RI 02912, USA*

1.1 Introduction

Magnetic nanomaterials have long been investigated due to their scientific and technological importance in many areas, such as magnetic data storage, magnetic fluids, catalysis, biomedicine, magnetic resonance imaging, hyperthermia, magnetic refrigeration, and environmental remediation [1–11]. The unique effects induced by the nanoscale distinguish the magnetism of the nanomaterials from their bulk counterparts. When a material is cut into smaller dimensions, the number of magnetic domains included in the material is decreased and magnetic coercivity is increased. When the size reaches a critical value, the material can only support a single magnetic domain and magnetic behavior of this single-domain material depends mostly on magnetization rotation. Depending on the magnetic characteristics, the single domain size of a material can be in tens, hundreds, or even thousands of nanometers. When the material dimension continues to shrink below the single domain size, surface atoms and temperature start to affect magnetic behaviors drastically and the material can become superparamagnetic at room temperature in which state it can be magnetized as a ferromagnetic material, but its magnetization direction is randomized by thermal agitation, showing zero remanent magnetization and no coercivity.

The key issues related to magnetic nanomaterials are in the synthesis with the desired size, shape, and structure controls. Due to the large surface area, surface energy, and magnetic dipolar interactions, magnetic nanomaterials should also be stabilized by a layer of organic or inorganic matrix. The coating chemistry developed further allows proper functionalization of these nanomaterials for varied applications. The controlled synthesis and coating for stabilization can now be realized from organic-phase synthesis protocols [12,13].

In this chapter, we summarize some widely explored magnetic nanomaterials of (i) metals and alloys, especially single metal M (M = Fe/Co/Ni) and their related alloys, such as MN (N = noble metal) and alloys of M_1M_2 (M_1, M_2 = Fe, Co, Ni); (ii) Fe/Co/Ni/Mn oxides; (iii) metal carbides and nitrides; (iv) rare earth (RE)-based

Magnetic Nanomaterials: Fundamentals, Synthesis and Applications, First Edition.
Edited by Yanglong Hou and David J. Sellmyer.

permanent magnets, specially RE-Fe (Co), RE-Fe (Co)-B, and RE-Fe (Co)-C/N magnets. In addition to the synthesis, we also review some of the common methods used to characterize these magnetic nanomaterials to better understand their phases, morphologies, micromagnetic structures, and bonding structures. We focus on the tools of X-ray magnetic circular dichroism (XMCD) spectroscopy, Lorentz transmission electron microscope and Mössbauer spectroscopy, magnetic extended X-ray absorption fine structure (MEXAFS), magnetic force microscopy (MFM), and superconducting quantum interference device (SQUID).

1.1.1 Typical Magnetic Nanomaterials

1.1.1.1 Magnetic Nanomaterials of Metal (Fe, Co, and Ni)

Fe, Co, and Ni are three common ferromagnetic elements that serve as structural backbones for tons of magnetic materials in our modern life. The common magnetic properties of Fe, Co, and Ni are given in Table 1.1. Study on the nanoscale Fe, Co, and Ni is both fundamentally and technologically important. With controlled stabilization and surface treatment techniques, these nanoscale materials can find many important applications, ranging from ferrofluids, biomedicine, to catalysis [14–16].

Synthesizing these nanomaterials with the desired dimension and property controls is critical for their practical applications. In the early stage (1950s), Fe was prepared in the nanoparticle (NP) form in mercury [18]. The improved methods involve the use of organic solvents for better Fe(0) protection and stabilization. The common precursor used to obtain metallic Fe is $Fe(CO)_5$. This is a metastable organometallic compound with the standard enthalpy of formation – 185 kcal mol^{-1} [19]. Despite its easy decomposition potential, it does have a complicated decomposition kinetics due to the formation of various clusters [20,21].

In general, utilizing the decomposition of $Fe(CO)_5$ to generate Fe nanomaterials can be accomplished by heat or sonication. Once produced, these nanomaterials need some proper protections to stay both chemically and colloidally stable for further applications, especially for biomedical applications [22]. Recent synthetic advances have allowed the preparation of monodisperse Fe NPs from the solution-phase reaction. For example, Sun and coworkers developed a simple one-pot reaction to produce monodispersed Fe NPs in the presence of oleylamine, as shown in Figure 1.1a and b [23]. Further studies indicate that the Fe growth process can be controlled by adding Cl ions, as these ions have a strong binding to the present NP surface and slow the Fe growth kinetics, and facilitate

Table 1.1 Properties of ferromagnetic Fe/Co/Ni elements with SI units [17].

Elements	σ_s/0 K, $A \cdot m^2 \cdot kg^{-1}$	σ_s/293 K, $A \cdot m^2 \cdot kg^{-1}$	T_c/K
Fe	222	218	1043
Co	162	161	1388
Ni	57	54	627

σ_s: saturation magnetization; T_c Curie temperature.

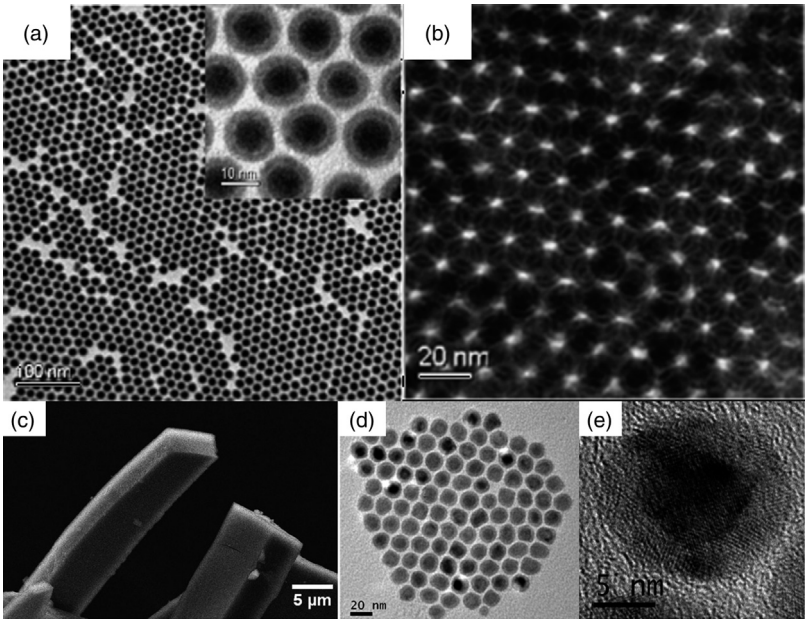

Figure 1.1 (a) TEM images of 4 nm/2.5 nm Fe@Fe_3O_4 NPs. Inset is HRTEM image of the Fe@Fe_3O_4 NPs. (b) Self-assembled Fe@Fe_3O_4 NPs superlattice. (c) SEM image of the platelike Fe NP assembly obtained directly from the synthesis solution. (d) TEM image of the 15 nm NPs obtained from the redispersion of the plate assembly in hexanes. (e) HRTEM image of a single NP revealing the metallic bcc-Fe core and Fe_3O_4 shell with Fe (110) and Fe_3O_4 (222) planes indicated [23,24]. Reproduced with permission of American Chemical Society.

the addition of Fe atoms in a thermodynamically more stable manner into better crystalline body-centered cubic (bcc) Fe, as shown in Figure 1.1c–e [24,25].

In addition to the decomposition of $Fe(CO)_5$, the metal–organic precursor Fe$[N(SiMe_3)_2]_2$ (Me = —CH_3) is also used for the generation of Fe NPs [26,27]. As reported by Chaudret *et al.*, the metal–organic precursor is decomposed in the presence of hexadecylamine (HDA) and a long-chain acid (oleic acid (OA) or hexadecylammonium chloride (HDAC)) under a H_2 atmosphere. The reaction gives bcc-Fe cubes with their M_s at 223 $A \cdot m^2 kg^{-1}$, which is close to the bulk value [26]. Fe$[N(SiMe_3)_2]_2$ can also be replaced by its dimers $\{Fe[N(SiMe_3)_2]_2\}_2$ and the decomposition in the presence of palmitic acid/HDA mixture produces ultrasmall (~1.5 nm) Fe(0) clusters, or polycrystalline spherical NPs with a mean diameter between 5 and 10 nm, or single nanocubes over 13 nm [28].

The reduction of iron salts can also generate Fe NPs. The reverse micelle method is commonly used for this reduction approach as the particle size can be better controlled by the micelle dimension [29,30]. For example, 3 nm Fe NPs were synthesized by using trioctylphosphine oxide (TOPO) as stabilizing agent, $Fe(AOT)_2$ (AOT = bis(2-ethylhexyl) sulfosuccinate) as iron precursor, and $NaBH_4$ as reducing media in an aqueous solution [31].

The methods developed for the synthesis of Fe NPs can be extended to the preparation of Co NPs as well. The metallic Co NPs in the size range of 1.8–4.4 nm show size-dependent blocking temperature, magnetic moments,

and hysteresis behaviors [32]. In addition, the morphology of the final products could also be tuned by varying the reaction parameters such as the reaction temperature [33]. Here, the Co particles nucleate and grow in the nanosized cages of inverse micelles formed by dissolving the surfactant molecules in an apolar solvent. Unfortunately, the size of the final products could not be precisely tuned by changing the water/surfactant ratio. To solve this problem, a germ-growth method is developed to verify that Co particles could be germinated in the first stage of the reaction as seeds, and then as nucleation sites to grow into larger particles [34]. The method leads to the formation of face center cubic (fcc)-Co NPs and their spontaneous 2D monolayer assemblies [35].

Benefiting from the nonthermodynamically controlled property of solution synthesis, monodisperse 9 nm Co NPs with the cubic symmetry of the β-phase of manganese (denoted as ϵ-Co) are synthesized by the reduction of $CoCl_2$ with lithium triethyl borohydride, as shown in Figure 1.2a and b. The as-synthesized ϵ-Co NPs are magnetically soft with reduced dipole interaction between the NPs, which is beneficial to stabilize the individual NPs during the size-selective process and facilitate the formation of ordered NP arrays [36]. In addition, the shapes of the Co NPs can be readily controlled by the NP structure. For example, hcp-Co nanodisks were obtained by the thermal decomposition of di-cobalt-carbonyl $Co_2(CO)_8$ in anhydrous *o*-dichlorobenzene (DCB) assisted with oleic acid [37]. A versatile pathway was proposed to tune the shape and the aspect ratio of Co nanocrystals to get Co nanorods through the decomposition of organometallic

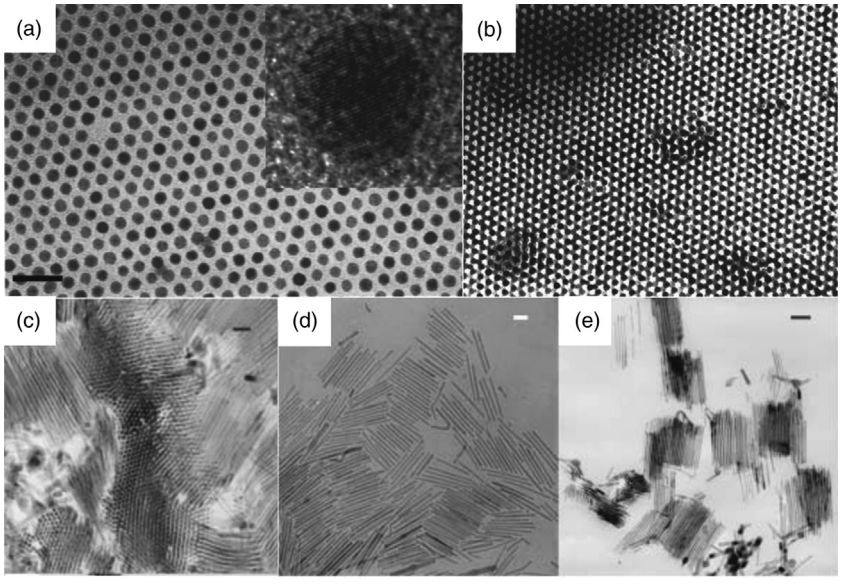

Figure 1.2 (a) TEM image of a 2D assembly of 9 nm cobalt NPs. *Inset:* High-resolution TEM image of a single particle. The scale bar is 48 nm. (b) TEM image of a 3D superlattice of 9 nm cobalt NPs assembled on amorphous carbon film at 70 °C. TEM micrographs of nanorods synthesized using hexadecylamine and (c) stearic acid, sample was prepared by ultramicrotomy, (d) lauric acid, and (e) stearic acid. The scale bar is 30 nm [36,38]. Reproduced with permission of AIP Publishing LLC.

precursors [Co(η^3-C_8H_{13})(η^4-C_8H_{12})] in anisole and via a self-organization process, as shown in Figure 1.2c–e [38,39].

Recent focus on Ni NPs is on their shape controls. It is widely accepted that the selective coordination of a special ligand on the initial nuclei is essential for the anisotropic growth [40–44]. However, the common ligands used for NP stabilization contain strong π-accepting characters, which degrades the magnetic performance of the NPs [45]. Recently, Pick and Dreysse suggested that the amine ligands might be a favorable alternative [46]. They studied the effects of hexadecylamine on the shape and magnetic properties of Ni NPs prepared by the reduction of $Ni(COD)_2$ (COD, cycloocta-1,5-diene). Results show that increasing the concentration of amines favors the growth of Ni nanorods and stronger ferromagnetism [47].

1.1.1.2 Magnetic Nanomaterials of MN Alloys (M = Fe, Co, and Ni, N = Noble Metal)

Nanomaterials of FePt alloys have long been a hot topic [48]. These FePt alloys can have a chemically disordered face-centered cubic (fcc) structure (commonly referred to as A_1 structure) and face-centered tetragonal (fct) structure (commonly referred to as L_{10} structure) [49]. The fct-FePt has a magnetocrystalline anisotropy constant K (measuring the ease of magnetization reversal) of 10^7 J m^{-3}, one of the largest among all known hard magnetic materials. This high K value arises from the unique layered Fe–Pt arrangement and strong spin–orbit coupling between Fe 3d and Pt 5d states along the Fe–Pt layer direction [50–52]. Also, the high K value endows Fe–Pt the thermal stable size down to around 2 nm, making them a promising candidate as high-density magnetic recording media [53]. FePt NPs are commonly prepared by thermal decomposition of $Fe(CO)_5$ and reduction of $Pt(acac)_2$, or by the coreduction of metal salts. Reduction of $Pt(acac)_2$ and decomposition of $Fe(CO)_5$ in the presence of OA and OAm around 300 °C can lead to the formation of monodisperse NPs with their size controlled from 3 to 10 nm and compositions controlled by the metal precursor ratios. As prepared, the FePt NPs often adopt the fcc structure. However, via thermal annealing at temperature higher than 500 °C, the fcc-FePt NPs with near 1/1 Fe/Pt atomic ratios can be converted to fct-FePt, as shown in Figure 1.3. The annealed FePt assemblies are ferromagnetic, supporting high-density magnetization reversal transitions [7]. To obtain the fct-structure at lower temperatures, the third element such as Ag, Cu, Sn, Pb, Sb, and Bi can be introduced [54–57].

FeAu alloys are also widely studied. Due to their limited solubility, the chemically ordered compounds in the FeAu bulk is not permitted when in a small size. However, the chemically ordered $L1_2$-type Fe_3Au and $FeAu_3$ compounds can be made to sub-10 nm NPs [58]. The *ab initio* first principle calculations suggest that Fe_3Au has a high saturation magnetization of about 143.6 emu g^{-1}, while $FeAu_3$ is antiferromagnetic with the net magnetization arising only from uncompensated surface spins [58]. In addition to FeAu alloys, the Au pyramids can also grow on highly faceted Fe NPs in an epitaxial growth manner [59].

In the case of CoPt, which is another magnetic system that is similar to FePt, the CoPt alloys have a high magnetocrystalline anisotropy of 4×10^7 ergs cm^{-3}, and a

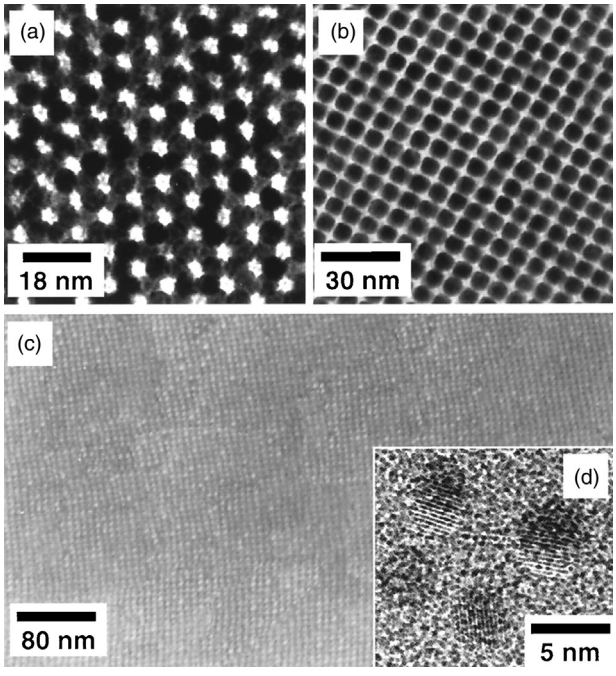

Figure 1.3 (a) TEM micrograph of a 3D assembly of 6 nm as-synthesized $Fe_{50}Pt_{50}$ particles deposited from a hexane/octane (v/v 1/1) dispersion onto a SiO-coated copper grid. (b) TEM micrograph of a 3D assembly of 6 nm $Fe_{50}Pt_{50}$ sample after replacing oleic acid/oleyl amine with hexanoic acid/hexylamine. (c) HRSEM image of a ~180 nm thick, 4 nm $Fe_{52}Pt_{48}$ NP assembly annealed at 560 °C for 30 min under 1 atm of N_2 gas. (d) High-resolution TEM image of 4 nm $Fe_{52}Pt_{48}$ NPs annealed at 560 °C for 30 min on a SiO-coated copper grid [7]. Reproduced with permission of the American Association for the Advancement of Science.

saturation magnetization of 800 emu cm^{-3} [60,61]. Modifying the syntheses of FePt NPs, various kinds of CoPt alloy nanomaterials can be obtained [62–64]. Understanding size, shape, and composition effects on the formation of the fct phase is necessary to develop hard magnetic FePt and CoPt. Takahashi *et al.* reported the size effect of fcc–fct ordering of FePt NPs by transmission electron microscopy (TEM). The study show that the ordering does not progress when the particle size has a diameter of less than 4 nm [65]. Concerning the morphologies of CoPt and FePt below 3 nm, *ab initio* calculations show that the ordered multiply twinned morphologies will not show hard magnetic behavior, which is in consistent with the experimental difficulties to stabilize the L_{10} phase in uncoated FePt NPs by thermal treatment [66–69].

When the alloys of CoPt, FePt, FePd, CoRn, and so on are in their state of chemically ordered structure, the highest value of K_u and the largest coercivity from each structure can be obtained [70–72]. Factors that influence the transition temperature T_C (order–disorder transition) have been further studied and size effects are found to dominate the structure ordering in FePt, FePd, and CoPt [73–81]. For example, 2.4~3 nm CoPt NPs can have a T_C in the range of 500–650 °C [82].

1.1.1.3 Magnetic Nanomaterials of M_1M_2 Alloys (M_1, M_2 = Fe, Co, and Ni)

When in an alloy state, the magnetic and mechanic properties are affected by the varied heteroelements, thus influencing their thermodynamic and elastic properties and phase stabilities. For example, when the Ni concentration is at about 35%, the thermal expansion coefficient of the fcc-FeNi steel vanishes, which is known as the Invar effect [83,84]. Exploring the magnetic and chemical order–disorder phenomena is necessary for the study of their intrinsic magnetism and certain important realistic effects such as chemical disorder-induced local lattice deformation [85–87]. Table 1.2 illustrates the magnetic ordering temperatures of various FeNi geometries.

The clusters are of special interests due to their unique role in the understanding of both magnetism and catalysis. For the FeNi clusters containing up to four Fe and four Ni atoms, magnetic moments per atom of these clusters are almost insensitive to the specific geometry, but in $Fe_{n-1}Ni$ ($n = 9$, 15, and 27) geometry similar to the bulk bcc structure, the clusters are ferromagnetic with magnetic moments higher than the bulk value [88]. Regarding the synthesis of FeNi alloy NPs, various methods have been introduced such as coprecipitation methods, reduction methods, direct current electrodecomposition, and sol–gel fabrication methods [89–93].

FeCo alloys, with high Curie temperature and high magnetization, are excellent soft magnetic materials for applications in magnetic sensors, magnetic recording head, motors, and generators in electric vehicles [94,95]. With the development of new synthetic techniques, the FeCo NP sizes, shapes, and compositions can now be well controlled, and shape anisotropy can be used to tune the FeCo into "hard" magnets (shape anisotropy can be estimated by coherent rotation mechanism $K_s = (\mu_0/4)\cdot M_s^2$, where K_s is the calculated room temperature anisotropy constant) [96]. As a result, the oriented FeCo wire arrays show a large coercivity (approximately 2800 Oe) and high squareness (approximately 0.9) [97]. Based on first-principles theory, it is found that the structurally distorted FeCo shows a uniaxial magnetic anisotropy energy (MAE) 50% larger than that of FePt [98]. This MAE increases enormously and reaches to a value on the order of 700–800 μeV/atom while in the state of *c/a* ratio of 1.20–1.25 and Co concentration of 60%. In addition, in the concentrations where the uniaxial MAE is very large, the magnetic moments is on the order of 2.1 μ_B, still a high value, as shown in Figure 1.4a. FeCo is also an efficient probe for magnetic heating, which can be used to improve the efficiency of chemotherapy and radiotherapy [99–102]. The

Table 1.2 Monte Carlo and measured magnetic ordering temperatures in Kelvin [85].

Alloy	Monte Carlo simulation			Measured	
	T_C random	T_C ordered	T_C equil	T_C random	T_C ordered
$FeNi_3$	870	1180	970	850	940
FeNi	820	1020	910	785	840
Fe_3Ni	520	580	580	\	\

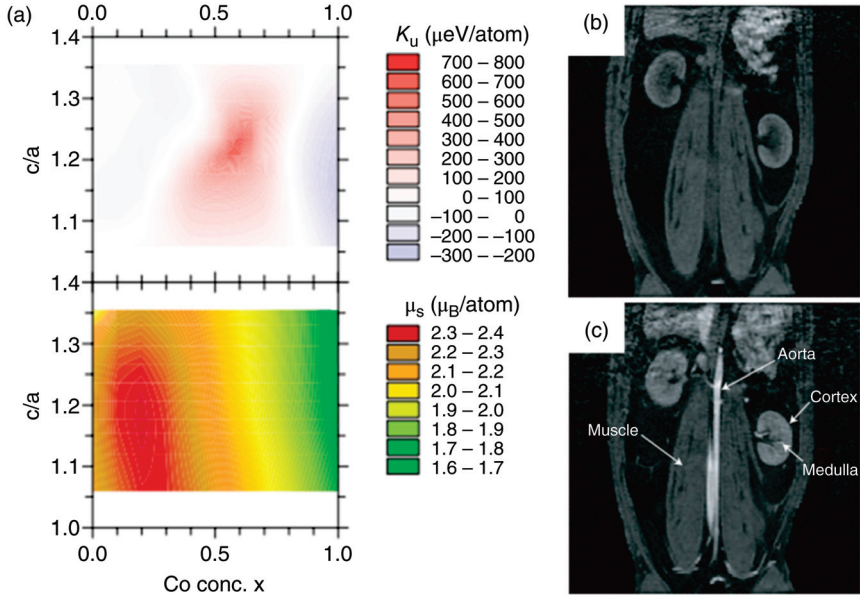

Figure 1.4 (a) Calculated uniaxial K_u (upper panel) and saturation magnetic moments (lower panel) of tetragonal $Fe_{1-x}Co_x$ as a function of the *c/a* ratio and the Co concentration *x*. (b and c) T_1-weighted MR images of a rabbit before (b) and 30 min after (c) initial injection of a solution of ~4 nm FeCo/single-graphitic-shell NPs (metal dose of about 9.6 μmol kg^{-1} for about 5 kg rabbit) [98,104]. Reproduced with permission of American Physical Society.

specific absorption rate (SAR) of magnetic materials in hyperthermia is given by $SAR = A \cdot f$, where A is the specific area of the hysteresis loop (specific losses) at the frequency f and magnetic field H at which the experiment is conducted. Under $H = 300$ Oe and $f = 310$ kHz, the FeCo nanowires have a SAR value of around 1500 W g^{-1} [103].

FeCo is also a sensitive probe for magnetic resonance imaging agent. Dai *et al.* prepared high-moment FeCo/single-graphitic-shell NPs that have r_1 and r_2 relativities of 70 and 644 mM^{-1} s^{-1}, respectively. The FeCo/single-graphitic-shell NPs also possess high optical absorbance in the near-infrared region, and show long-circulating positive-contrast enhancement at low metal dosages, as shown in Figure 1.4b and c [104].

Nanowires of CoNi alloys can also be prepared by separating nucleation and growth steps in the synthesis to show large coercivity [105]. Tuning the Co composition in CoNi nanowires enables the control of the effective anisotropy determined by the balance between the hexagonal close-packed (hcp) and fcc magnetocrystalline and shape anisotropy [106,107].

1.1.1.4 Magnetic Nanomaterials of Carbides and Nitrides M–C/N (M = Fe, Co, and Ni)

The electron-rich M–C/N (M = Fe, Co, and Ni) bonding endows carbides and nitrides with peculiar magnetic, catalytic, and electronic properties [108–113]. The origin use of carbide nanostructures initiate from the usage of Damascus

steel [114]. Regarding the iron carbides compounds, the complex phase diagrams attract wide theoretical and experimental interests. From the perspective of Fe-C based molecules, the geometry and electronic structures of various neutral and ionic Fe-C clusters were reported, including Fe_2C [115,116], FeC_n ($n = 2–5$) [117], $Fe_nC/Fe_nC^+/Fe_nC^-$ ($n = 1–6$) [118,119], and clusters with greater carbon entities content FeC_n ($n = 1–4$), Fe_2C_n ($n = 1–3$) [120,121]. From the perspective of theoretical simulation results, the strong Fe—C bonding reduces the local magnetic moment of Fe atoms [122]. In a recent study by Hou *et al.*, varied phases of iron carbide NPs of hexagonal (hexa) and monoclinic (mono) Fe_2C, monoclinic Fe_5C_2, and orthorhombic (ortho) Fe_3C NPs were presented utilizing a "seed conversion" manner. All the NPs are in a near monodisperse state, with the highest saturation magnetization M_s value of 101.2 emu g^{-1} and the highest Curie temperature T_C of 497.8 K. All the obtained NPs exhibit lower M_s than that of the bcc-Fe NPs, which is in accordance with the theoretical simulations, as shown in Figure 1.5 [123].

Recently, the Co_2C and Co_3C nanomaterials are synthesized possessing unusually large coercivities and energy products. Through first-principles electronic structures study using GGA + U functional, it is suggested that the C atom intercalation is responsible for the magnetic anisotropy enhancement [124,125].

The nitrides magnetic nanomaterials are also fascinating areas with their unique catalytic and magnetic properties. Regarding the magnetic properties of iron nitrides, various phases such as $Fe_{16}N_2$, Fe_4N, Fe_3N, Fe_2N, and mononitride FeN possess complicated magnetic properties from ferromagnetic to antiferromagnetic and nonmagnetic, and are considered to be potential in nanomagnetism and spintronic areas [126]. Perhaps the most amazing magnetism is in $Fe_{16}N_2$, in which the most distant Fe atoms from the N atoms possess the large 3d hole in both the down-spin and up-spin states [127]. It is suggested that the penetration of N atoms expanded the Fe lattice with enhanced magnetic moments in terms of hopping electrons and preventing the exchanged splitting. Regarding nickel carbides and nitrides, the distinctions between Ni_3C and hcp-Ni are the most debating topic. Taking into consideration the early reported hexagonal lattice ($a = 2.628$ Å, $c = 4.308$ Å), the results that Ni_3C is of rhombohedral lattice

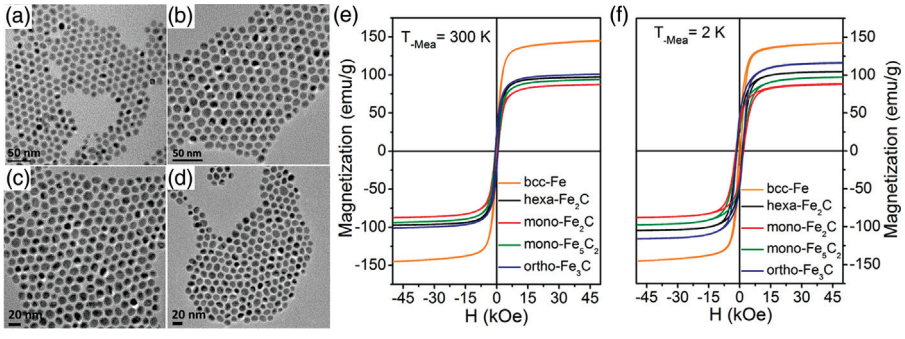

Figure 1.5 TEM images of hexa-Fe_2C (a), mono-Fe_2C (b), mono-Fe_5C_2 (c), and *ortho*-Fe_3C (d). *M* versus *H* curves at 300 K (e) and 2 K (f) of the initial bcc-Fe and the preformed iron carbide NPs [123].

($3R^-$, $a = 4.553$ Å, $c = 12.92$ Å) are very different, while other reports show that the Ni_3C possesses the orthorhombic cementite-type structure [128–130]. The intrinsic magnetism are also debated with reported results from ferromagnetic to nonmagnetic [131–134]. It has been reported that the electron transformations from the Ni 3d states to the C 2p band promoted the forced exchange splitting in the case of ferromagnetic solution with the Fermi level at the upper part of the Ni 3d states [135]. With the increased C concentrations in Ni—C bonding, the calculated magnetic moment decreases and quenches at a critical value. In the case of Ni—N bonding, the fcc-$NiN_{0.125}$ and fcc-$NiN_{0.25}$ with the Ni sublattice exhibiting little distortion from the fcc lattice possess significant local magnetic moments [135].

1.1.1.5 Magnetic Nanomaterials of Metal Oxides

Iron oxides are widespread in nature, due to their special properties such as low toxicity, robust chemical stability, high corrosion resistance and excellent magnetic properties [12]. Fe_3O_4 has a cubic inverse spinel structure. The lattice constant of Fe_3O_4 crystal is $a = 0.839$. The unit cell of Fe_3O_4 has 32 O^{2-} ions that are regular cubic close-packed along the [111] direction. Also, the Fe_3O_4 crystal structure includes two different iron sites: tetrahedral sites made up of Fe^{3+} and octahedral sites made up of both Fe^{2+} and Fe^{3+} [136]. Based on its unique structure, recent research on Fe_3O_4 has attracted much attention for its fundamental nanomagnetism and its potential applications [137,138]. Researchers have developed various methods to synthesize iron oxides. The most widely used methods are based on organic-phase synthesis [13,138]. Park *et al.* have synthesized monodisperse Fe_3O_4 NPs by a thermal decomposed method [139]. In their synthesis, metal chloride first reacts with Na–oleate and metal–oleate complex with NaCl is obtained. Thereafter, metal–oleate complex is mixed with octadecene and heated to more than 300 °C and the metal–oleate decomposes into metal oxide with monodisperse morphology. Sun *et al.* have reported a simple process for preparing monodisperse FeO NPs through a high-temperature reaction of $Fe(acac)_3$ with oleic acid and oleylamine. The sizes of the NPs are tunable from 10 to 100 nm and the shapes can be controlled to be either spherical or truncated octahedral [140]. Under controlled annealing conditions, the as-synthesized FeO NPs are converted into Fe_3O_4, γ-Fe_2O_3, α-Fe_2O_3, or they undergo disproportionation to form Fe–Fe_3O_4 composite NPs. These chemical conversions of the paramagnetic FeO NPs facilitate the one-step production of various iron-based NPs with controlled sizes and tunable magnetic properties for various nanoscale magnetic and catalytic applications.

Cobalt oxide has three types of common polymorphs: monoxide or cobaltous oxide (CoO), cobaltic oxide (Co_2O_3), and cobaltosic oxide or cobalt cobaltite (Co_3O_4). Co_3O_4 has a spinel-type structure consisting of both Co^{2+} and Co^{3+}, which is the most stable cobalt oxide. It is a simple as well as an efficient way of preparing cobalt oxide (Co_3O_4) NPs by precipitation. In a report by Agilandeswari and Rubankumar, Co_3O_4 NPs with agglomerated assembled spheres are synthesized, the magnetic characterizations exhibit weak ferromagnetic behavior [141].

Commonly, nickel oxides have three types: NiO, NiO_2, and Ni_2O_3. By changing the synthesis condition and methods, one can obtain nickel oxides in different crystalline phases, such as monoclinic, cubic, hexagonal, and rhombohedral

crystals [142]. Song *et al.* used nickel ethylene glycol as the precursor, successfully synthesized flower-like NiO. The NiO nanoflowers show a very small hysteresis loop with a H_c of 100 Oe and a M_r of 0.015 emu·g^{-1}, indicating a typical ferromagnetic behavior [143].

Manganese oxides have several different forms of MnO, MnO_2, Mn_2O_3, and Mn_3O_4. MnO_2 has several crystalline structures, including α-MnO_2, β-MnO_2, γ-MnO_2, and δ-MnO_2. Previous methods to prepare MnO_2 include thermal decomposition, electrodeposition, physical mixing, sol–gel, and microwave-assisted synthesis [144]. Moreover, by controlling the reactant concentration, reaction temperature, and reaction time, MnO_2 with different sizes and structures were obtained, and nanobelts, nanowires, flowerlike, and tubular architectures were also reported [145–147]. Magnetic susceptibility of MnO between room temperature and about 130 K follows a Curie–Weiss type of behavior, while that of Mn_3O_4 is strongly enhanced over MnO due to the larger effective moment (theoretical $\mu_{eff} = 9.15\,\mu_B$) [148].

1.1.1.6 Rare Earth-Based Permanent Magnets

The focus for the development of permanent magnets lies in the increase of reliability, strength, and ability to store energy, which are characterized by the energy product – $(BH)_{max}$ (the key figure of merit of permanent magnets) [149]. During the past decades, the $(BH)_{max}$ has been enhanced, starting from about 1 MGOe for steels to about 3 MGOe for hexagonal ferrites, and finally reaching to about 56 MGOe for neodymium–iron–boron magnets [150].

$SmCo_5$, Sm_2Co_{17}, and $Nd_2Nd_{14}B$ are well-known rare earth (RE) permanent magnets. SmCo alloy magnets have a high $(BH)_{max}$ ranging from 14 to 28 MGOe and better temperature characteristics than the NdFeB magnets at higher temperature working conditions (Curie temperature of 750 °C for $SmCo_5$, more than 800 °C for Sm_2Co_{17}, compared with about 400 °C for $Nd_2Fe_{14}B$ and 465 °C for ferrite) [149]. $SmCo_5$ is one of the most important hard magnets among the SmCo-type permanent magnets, the crystalline structure is shown in Figure 1.6. Regarding the preparation of Sm-Co magnets, Hou *et al.* have prepared $SmCo_5$ by a facile chemical method, just annealing the core/shell-structured Co/Sm_2O_3 NPs at high temperatures [151]. The results show that the product has a H_c as high as 24 kOe (1 kOe = 0.08 A m^{-1}) at 100 K and 8 kOe at room temperature, while the remnant magnetic moment keeps 40–50 emu g^{-1}. Recently, the 2 : 17 type SmCo permanent magnets (namely, Sm_2Co_{17}) have also

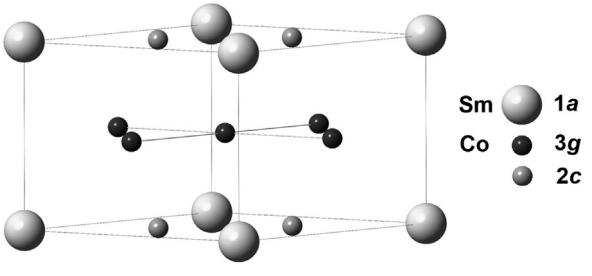

Figure 1.6 The crystal structure of $SmCo_5$.

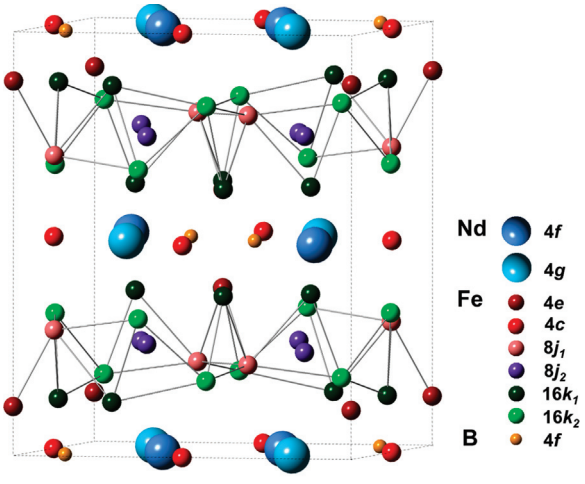

Figure 1.7 The crystal structure of $Nd_2Fe_{14}B$.

attracted much attention due to their superior magnetic properties and excellent thermal stability [149,152].

Chaban *et al.* investigated the phase diagram of Nd–Fe–B near the composition 2 : 14 : 1 in 1979; afterward, the composition and crystal structure of $Nd_2Fe_{14}B$ was confirmed. The structure of the typical compound $Nd_2Fe_{14}B$ is shown in Figure 1.7, in which Fe nets providing high magnetization are layered with RE elements (Nd) [153,154]. Today Nd–Fe–B magnets are the leading RE permanent magnets, due to their high coercivity and large $(BH)_{max}$. There are several methods to prepare Nd–Fe–B magnets, for example, sintering, melt spinning, hydrogen treating Nd–Fe–B alloys, mechanical alloying, or hot working [149].

Taking into consideration that the Sm-Co and Nd-Fe-B magnets contain costly Co and Nd elements, the research of low-cost permanent magnets is necessary. Sm-Fe-N(C) magnets have attracted much attention owing to their excellent magnetic properties such as high-saturation magnetization. In the 1990s, Coey *et al.* found that R_2Fe_{17} could change to $R_2Fe_{17}N_x$ by absorbing N_2 above 300 °C in a solid–gas reaction. N atoms enter the unit cell of R_2Fe_{17} as interstitial atoms, and the unit cell can sustain Th_2Zn_{17} or Th_2Ni_{17} structure [155]. The anisotropy field at room temperature is 14 T, almost twice of that of $Nd_2Fe_{14}B$.

1.2 Typical Characterization of Magnetic Nanomaterials

1.2.1 X-Ray Magnetic Circular Dichroism Spectroscopy

The X-ray magnetic circular dichroism, which consists of the difference in absorption of left- and right-circularly polarized X-rays, has evolved over 25 years, with the physics similar to the UV-vis MCD known from 1897 [156]. It possesses great advantage in the detection of elemental specificity coming with

the core electron spectroscopies, and in proving quantitative information about the distribution of spin and orbital angular momenta. Moreover, the XMCD also finds its strength in the capacity of determining spin orientations and inferring spin states from magnetization curves, and in the ability of separating magnetic and nonmagnetic entities [157,158]. The key ingredients of XMCD consist of a source of circularly polarized X-rays, a monochromator and optics, and the X-ray absorption detection system. To extend the strength of XMCD, the spatially resolving instruments are often introduced to obtain element-specific images of magnetic properties [159,160]. Generally, the combined microscopes are divided into three categories: (i) recording the transmission or secondary yield of fluorescence or photoelectrons by a scanning apparatus, in which a focused X-ray spot is raster-scanned across the examined sample; (ii) operating in a mode similar to transmission light microscopes, in which the condenser and analyzer lenses are replaced by zone plates for the X-ray region; (iii) imaging the photoelectron yield from different regions of the sample utilizing the electron microscope optics, as shown in Figure 1.8 [157].

Utilizing the XMCD, the valence, and spin states in spinel $MnFe_2O_4$ was reported [161]. It is declared that there exist Fe_A^{3+} (T_d) ions in $MnFe_2O_4$ by comparing the XMCD spectrum with that of $GaFeO_3$ and γ-Fe_2O_3, and an inversion of about 10% of Fe ions from B (O_h) sites to A (T_d) sites, as shown in Figure 1.9.

1.2.2 Lorentz Transmission Electron Microscope

Lorentz transmission electron microscope (LTEM) has been intensively investigated to explore the magnetic domain structure and magnetization reversal mechanisms for more than 40 years. When utilizing a TEM to analyze the magnetic domain structures, it is suggested that many applicable magnetic properties are extrinsic rather than intrinsic [162,163]. The difficulty encountered when utilizing a TEM to study the magnetic materials is that the specimen is usually immersed in the high magnetic field of the objective lens [164]. In order to solve this problem, numerous ways are proposed: (i) switching off the standard objective lens; (ii) changing the position of the specimen; (iii) changing the pole pieces to retain the specimen in its standard position, and once again to provide a nonimmersion environment; (iv) adding super minilenses in addition to the standard objective lens and once again switching off [163,165–168].

The LTEM is a sufficient way of observing domain-wall pinning and motion [169]. Besides, the LTEM also finds its role in the detection of topological spin textures. For example, the skyrmion is a vortex spin structure in which the spins pointing in all directions are wrapped to a sphere and is characterized by a topological number of -1 that was first found in B20-type MnSi [170–176]. Generally, the skyrmions are stabilized in the chiral crystal structure and tend to crystallize basically in a hexagonal lattice or tetragonal/cubic lattice form [177]. Except for small-angle neutron diffraction study, skyrmions could be directly observed by LTEM in B20-type alloys [178]. In a study by Seki *et al.*, magnetoelectric skyrmion in an insulating chiral–lattice magnet Cu_2OSeO_3 was observed by LTEM, and the skyrmion could magnetically induce electric polarization, as shown in Figure 1.10 [170].

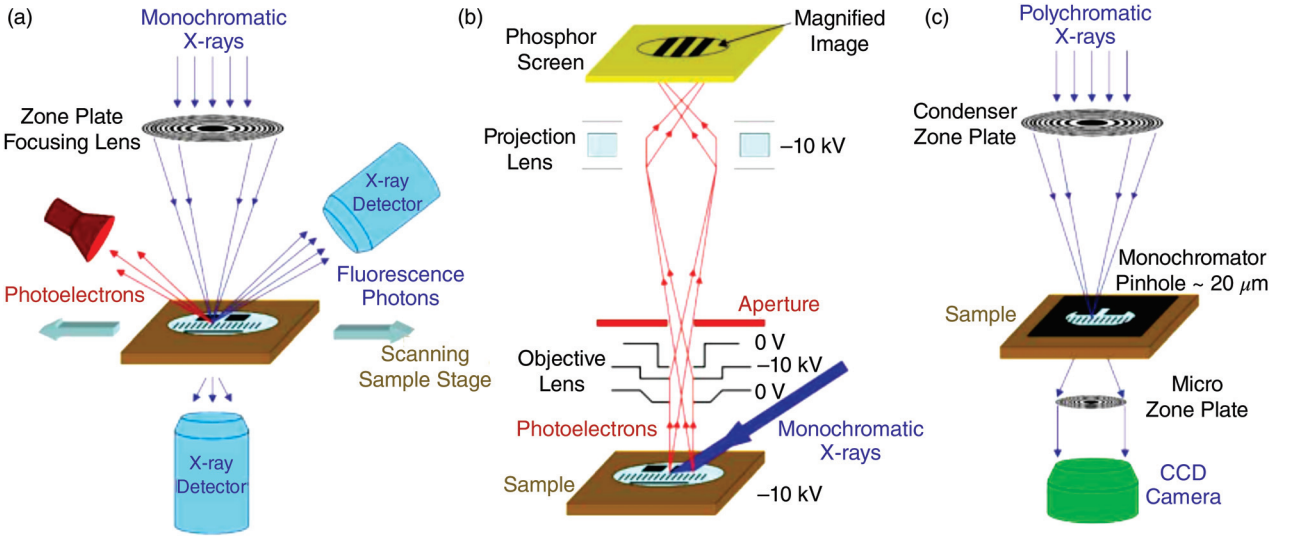

Figure 1.8 Schematic illustration of (a) a scanning X-ray microscope, (b) a photoelectron microscope, and (c) an imaging transmission microscope [157]. Reproduced with permission of Elsevier.

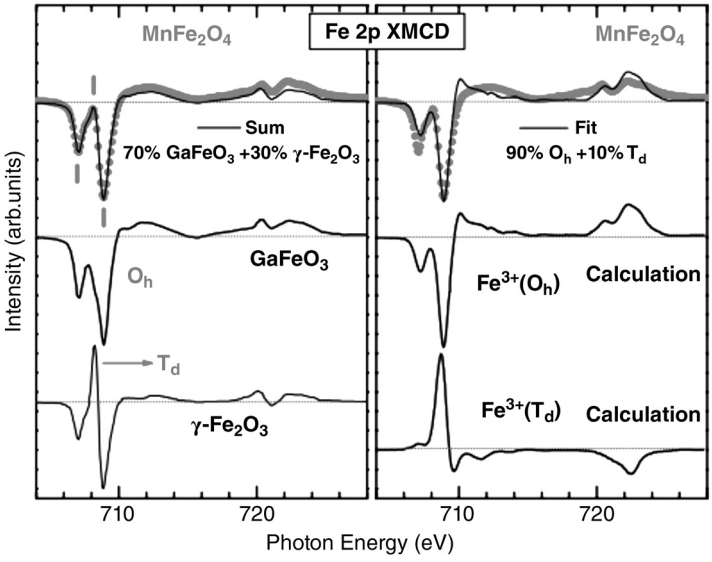

Figure 1.9 Comparison of the Fe 2p XMCD spectrum of $MnFe_2O_4$ with those of γ-Fe_2O_3 and $GaFeO_3$ (*left*) and their weighted sum (*left*) and also those of the calculated Fe 2p XMCD spectra for Fe_B^{3+} (O_h) and Fe_A^{3+} (T_d) and their weighted sum (*right*) [161]. Reproduced with permission of American Physical Society.

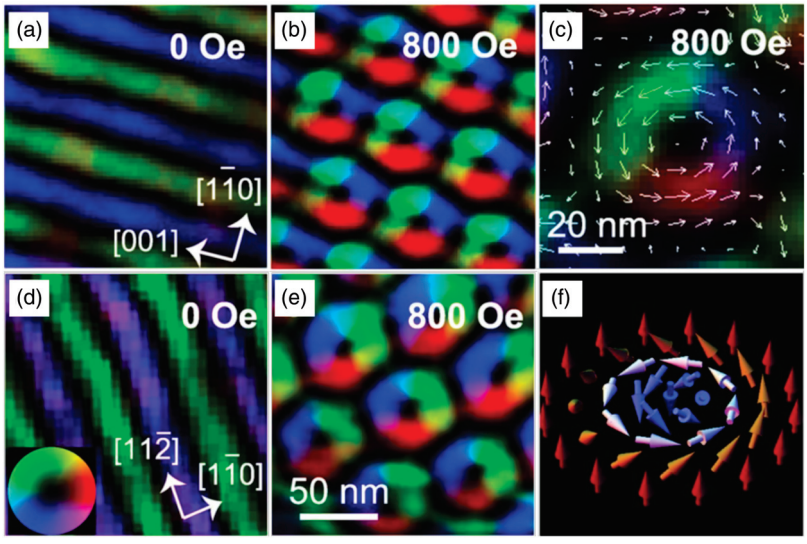

Figure 1.10 (a–e) Lateral magnetization distribution map for a thin film (~100 nm thick) sample of Cu_2OSeO_3, obtained through the analysis of Lorentz TEM data taken at 5 K. The color wheel in the bottom-left corner of part (d) shows the direction (hue) and relative magnitude (brightness) of the lateral magnetization. Panels (a and b), as well as (d and e), represent images for the (110) and (111) planes, respectively, and a magnetic field is applied normal to the observed sample plane. In both cases, proper screw-spin texture appears for zero magnetic field, whereas a skyrmion lattice with the identical spin chirality is formed for $H_c = 800$ Oe. A magnified view of part (b) is shown in part (c), where white arrows represent the magnetization direction. (f) Schematic illustration of a single magnetic skyrmion [170]. Reproduced with permission of John Wiley & Sons.

1.2.3 Mössbauer Spectroscopy

Mössbauer spectroscopy, which is the recoilless emission and resonant absorption of the γ-ray in the nucleus, has made great contributions to the development in solid-state science, bioscience, metallurgy, and mineralogy. Since the year 1956, when Rudolf Mössbauer conducted the experiments concerning the scattering of the 129 keV γ-ray of ^{191}Ir, who was then awarded the Nobel Prize in 1961, Mössbauer effects have been intensively investigated [179–184]. The ^{57}Fe is found to be the most suitable nucleus for the recoilless resonance. In Mössbauer spectroscopy research, the hyperfine interactions of the nucleus are typical, in which the nuclear levels are affected by the magnetic fields and the electronic charge through Coulomb interactions [182,183]. The first observed spectrum was reported by Kistner and Sunyar, reflecting all three types of hyperfine interactions between nuclear moments and electrons concerning the magnetic hyperfine splitting of α-Fe_2O_3 [185]. Mössbauer spectroscopy are powerful tools in the investigations of transition metal compounds, especially on the bonding and structural properties, valence state, solid-state reactions, electron transfer reactions, mixed valency, spin crossover, and magnetic properties [180]. The three hyperfine characteristics are of vital importance to determine the different Fe species if using ^{57}Fe Mössbauer spectrometry [179]. Due to its efficiently local probe sensitivity, the ^{57}Fe Mössbauer spectrometry provides rich characteristics of the local atomic order, such as detection of chemical homogeneity of intraparticles and interparticles, differentiation of surface/core Fe species, and superparamagnetic fluctuations, particularly in the ferromagnetic, antiferromagnetic, and ferromagnetic systems. The obtained spectra often had broadened and overlapped lines exhibiting both the magnetic sextets and the quadrupolar doublets, which are temperature dependent. For example, the chemically homogeneous magnetite Fe_3O_4, of which a Verwey transition (metallic insulating transition) appears at about 120 K, and the magnetic properties relate to metal–oxygen stoichiometry [186–189]. Two well-resolved magnetic sextets are shown in the Mössbauer spectrum, of which the outer sextets are attributed to Fe^{3+} ions located in tetrahedral site and the inner spectra correspond to both the Fe^{2+} and Fe^{3+} ions in the octahedral sites, as shown in Figure 1.11 [179].

1.2.4 Magnetic Extended X-Ray Absorption Fine Structure

The extended X-ray absorption fine structure (EXAFS) with unpolarized or linearly polarized X-rays has long been a well-established technique of short-range order to investigate the structural and bond properties of bulk solid materials, surfaces and interfaces, and films and molecules [190]. The EXAFS modulates the photoabsorption cross section of the ejected photoelectron with the one that is scattered by the surrounding atoms. In the analysis and interpretation of EXAFS with nonpolarized or linearly polarized X rays, only the Coulomb interaction is considered for the elastic and inelastic scattering process and the backscattering amplitude [191]. It has been demonstrated that the near-edge absorption of circularly polarized X rays depends on the spin polarization of the photons, which is relative to the spin polarization of the magnetic electrons on the absorber in the case of magnetized

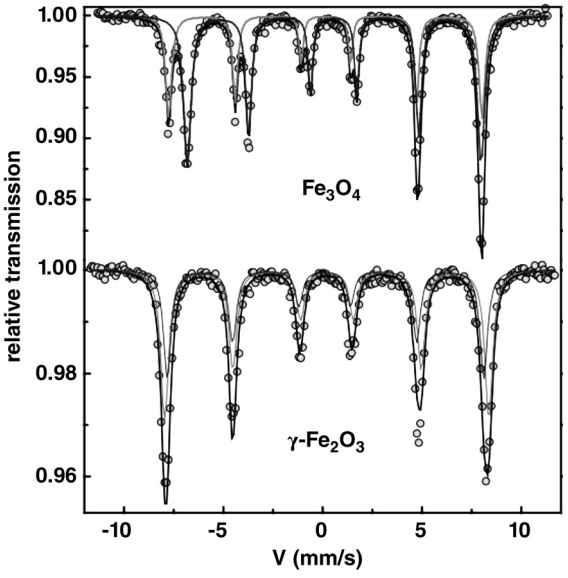

Figure 1.11 Typical 300 K Mössbauer spectra of microcrystalline magnetite (*up*) and maghemite (*down*) [179]. Reproduced with permission of Springer.

targets [191–194]. Thus, if the absorber is magnetized in the direction of **k** vector, the electrons of the magnetic neighboring atoms are also partially spin polarized, and the exchange potential is present except for the Coulomb potential in the scattering process [191]. It is particularly expected that the magnetic EXAFS will give additional information on the distribution and magnitude of magnetic moments around the absorber atoms. Researcher has realized from the very beginning that the physical origin of the occurrence of the XMCD in the EXAFS region is the same as in the X-ray absorption near-edge structure (XANES) region. For example, through the analysis of the *K*-edge spectra of Ni in fcc-Ni and $L_{2,3}$-edge spectra of Pt in Fe_3Pt, the MEXAFS spectra can be interpreted in terms of the local electronic structure of the absorbing atom, although information on the magnetic properties of the absorbing atom could not be fully derived [195].

1.2.5 Magnetic Force Microscopy

Since the late 1980s, the magnetic force microscopy (MFM) has been most widely used technique in magnetism research both academically and industrially, especially in the field of recording media [196,197]. Shortly after the invention of atomic force microscope (AFM), it is recognized that the detection of magnetostatic interactions at a local scale is possible by operating the noncontact scanning force microscope. Generally, the MFM is equipped with a ferromagnetic probe, and easily raster-scan across any ferromagnetic targets. In fact, the MFM is very applicable and easy to perform under various environmental conditions due to the independent characteristic of the near-field magnetostatic interaction with the surface contamination [198].

The MFM is first demonstrated on a magnetic recording head, and then is expanded to the analysis of individual interdomain boundaries and internal fine structures. Now the MFM are also employed in imaging flux lines in superconductors, detection of magnetic interactions to eddy currents, and dissipation phenomena [199–202]. Despite the facile characteristic of MFM, the raster-scanning of sample is much slower compared to the magnetization reversal in terms of time range, but it is possible to observe quasistatic magnetization reversal process by MFM with carefully optimized setup. By successively decreasing the applied field, the magnetization reversal properties of 60 nm Fe nanowires are investigated utilizing an in-field MFM; the resulting MFM images show that the magnetization undergoes a sharp reversal at various angles, which is described by a curling model [203].

MFM is also efficient in the research of spin-ice materials. In the research of spin-ice materials, the magnetic dipole is divided into a positive and negative magnetic charge ($\pm q$) separated by one lattice spacing [204–206]. As reported by Ladak *et al.*, the MFM is utilized in the imaging of monopole defects on the spin-ice lattice of two-dimensional Co honeycomb nanostructures. In their study, the movement of magnetic charge is demonstrated, as shown in Figure 1.12 [207].

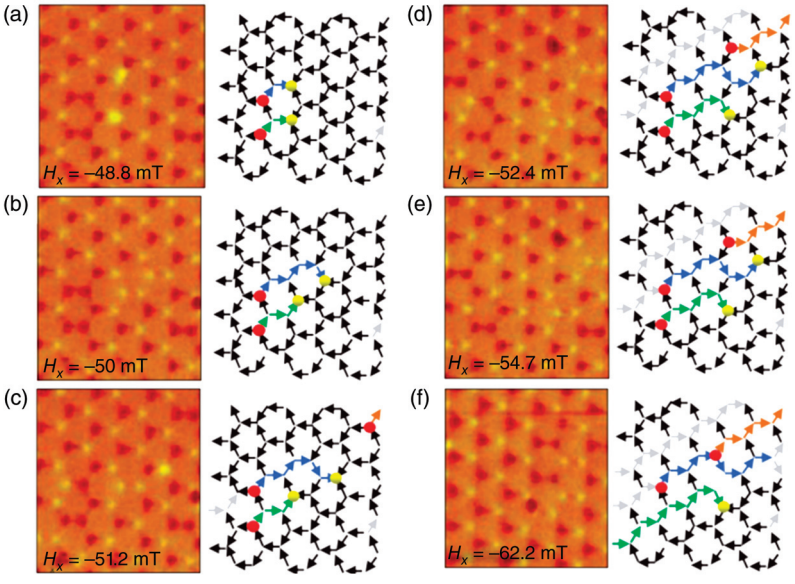

Figure 1.12 The movement of magnetic charge. MFM images in zero field after the labeled conditioning fields. (a) Two 3 in. monopole defects with $Q = +3q$ form (bright yellow spots, yellow dots), with strings of head–tail spins (blue and green) to opposite magnetic charges $1Q = -2q$ (red dots). Further bar flips are required to make the schematic (*right*) match the observed data; the gray arrows indicate a (nonunique) trial solution. (b) The $1Q = +2q$ magnetic charges hop to the right, changing from $Q = +3q$ to $Q = +q$. (c–f) Another $1Q = -2q$ magnetic charge appears, tracing its own (orange) string to the left, until it is blocked by the blue string of the $1Q = +2q$ carrier [207]. Reproduced with permission of Nature Publishing Group.

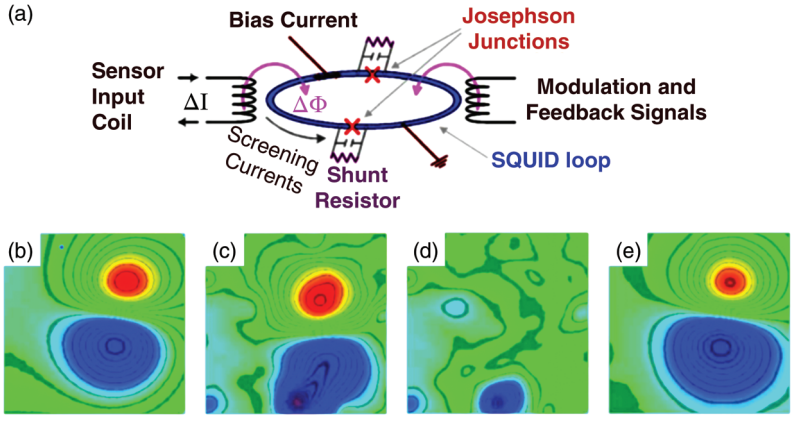

Figure 1.13 (a) Dual junction DC SQUID loop. The capacitor represents the self-capacitance of the junction. (b–e) Magnetic field maps of a room-temperature embedded strain sensor under a 4 cm thick concrete overcoating. (b) Bare sensor showing dipole characteristics. (c) Sensor under concrete. (d) Bare concrete. Image (e) = c–d is a digital subtraction of C and D showing that it is possible to image objects deep underneath magnetically complex coverings. The scans cover a $6 \times 6\,cm^2$ area [208]. Reproduced with permission of AIP Publishing LLC.

1.2.6 Magnetic Analysis

There are numerous ways to measure and evaluate the magnetic fields and performances based on varied sensing methods from microtesla to picotesla. The most sensitive magnetic flux detector is the superconducting quantum interference device (SQUID) operating at cryogenic temperatures with quantum-limited sensitivity of field resolution at the 10^{-17} T level [208–210].

The SQUID is also the most sensitive for detecting the magnetic field at low frequencies (<1 Hz), which is based on the remarkable interactions of the electric currents and magnetic fields detected. Meissner effect and the Josephson effect are commonly mentioned in superconducting quantum devices. In fact, the SQUID is a ring of superconductor interrupted by one or more Josephson junctions, which offers the ability to measure magnetic signals, as shown in Figure 1.13a. The SQUID is configured to measure a wide variety of electromagnetic properties, such as DC and AC measurements of varied magnetic materials. The nuclear magnetic resonance (NMR) signals could also be obtained, in this situation, targets such as protons or ^{19}F are placed in the center of SQUID detection coils and then the external field sweeps or an excitation is applied to the sample [211]. Due to the vector properties, the SQUID is also utilized for the detection of rotational movement of a magnetometer coil in the earth's magnetic field (about 50 μT) as small as 10^{-3} arc s [212,213]. The stress and strain are also of significant importance on the magnetic properties, in which the SQUID also finds its role, as shown in Figure 1.13b–e [208].

1.3 Conclusions

The magnetic nanomaterials are fascinating and have fertile applications in various of fields. There are great progresses in the synthesis of magnetic nanomaterials with controlled size, shape, and relevant properties so far. To carry out the applications of these magnetic nanomaterials, the large-scale synthesis method for industry level should be developed. Furthermore, to meet the requirements of next-generation electric devices, new type of advanced magnets should be found through the combination of the fundamental of magnetism, materials science, engineering, and nanotechnology. On the other hand, with the development of advanced facilities, it is expected to get insight of the structure and intrinsic properties of magnetic nanomaterials. With the deep understanding of structure and properties, it will enable us to design and fabricate advanced magnetic nanomaterials based on various requirements of industries.

References

1 Na, H.B., Song, I.C., and Hyeon, T. (2009) *Adv. Mater.*, **21** (21), 2133–2148.
2 Chikazumi, S., Taketomi, S., Ukita, M. *et al.* (1987) *J. Magn. Magn. Mater.*, **65** (2–3), 245–251.
3 Lu, A.H., Schmidt, W., Matoussevitch, N. *et al.* (2004) *Angew. Chem.*, **116** (33), 4403–4406.
4 Gupta, A.K. and Gupta, M. (2005) *Biomaterials*, **26** (18), 3995–4021.
5 Mornet, S., Vasseur, S., Grasset, F. *et al.* (2006) *Prog. Solid State Chem.*, **34** (2), 237–247.
6 Takafuji, M., Ide, S., Ihara, H. *et al.* (2004) *Chem. Mater.*, **16** (10), 1977–1983.
7 Sun, S., Murray, C., Weller, D. *et al.* (2000) *Supramol. Sci.*, **287** (5460), 1989–1992.
8 Pecharsky, V.K. and Gschneidner, K.A. Jr. (1999) *J. Magn., Magn., Mater.*, **200** (1), 44–56.
9 Tsang, S.C., Caps, V., Paraskevas, I. *et al.* (2004) *Angew. Chem.*, **116** (42), 5763–5767.
10 Elliott, D.W. and Zhang, W.-X. (2001) *Environ. Sci. Technol.*, **35** (24), 4922–4926.
11 Yang, W., Rehman, S., Chu, X. *et al.* (2015) *ChemNanoMat*, **1** (6), 376–398.
12 Hyeon, T. (2003) *Chem. Commun.*, (8), 927–934.
13 Wu, L., Mendoza-Garcia, A., Li, Q. *et al.* (2016) *Chem. Rev.*, **116** (18), 10473–10512.
14 Blanchard, M. and Derule, H., Canesson, P. (1989). *Catal. Lett.*, **2** (5), 319–322.
15 Hai, N.H., Lemoine, R., Remboldt, S. *et al.* (2005) *J. Magn. Magn. Mater.*, **293** (1), 75–79.
16 Huber., D.L. (2005) *Small*, **1** (5), 482–501.
17 Weast, R.C., Astle, M.J., and Beyer, W.H. (1988) *Handbook of Chemistry and Physics*;, CRC Press, Boca Raton, FL.
18 Luborsky., F. (1957) *J. Phys. Chem.*, **61** (10), 1336–1340.
19 Haynes, W.M. (2016) *CRC Handbook of Chemistry and Physics*, Taylor & Francis.

20 Giesen, A., Herzler, J., and Rot, P. (2003) *J. Phys. Chem. A*, **107** (26), 5202–5207.
21 Wen, J.Z., Goldsmith, C.F., Ashcraft, R.W. *et al.* (2007) *J. Phys. Chem. C*, **111** (15), 5677–5688.
22 Pankhurst, Q.A., Connolly, J., Jones, S. *et al.* (2003) *J. Phys. D Appl. Phys.*, **36** (13), R167.
23 Peng, S., Wang, C., Xie, J. and Sun, S. (2006) *J. Am. Chem. Soc.*, **128** (33), 10676–10677.
24 Zhang, S., Jiang, G., Filsinger, G.T. *et al.* (2014) *Nanoscale*, **6** (9), 4852–4856.
25 Lacroix, L.-M., Huls, N.F., Ho, D. *et al.* (2011) *Nano Lett.*, **11** (4), 1641–1645.
26 Dumestre, F., Chaudret, B., Amiens, C. *et al.* (2004) *Supramol. Sci.*, **303** (5659), 821–823.
27 Renaud, P. and Fejes, P. (1997) *Chem. Mater*, **9**, 3060.
28 Meffre, A., Lachaize, S., Gatel, C. *et al.* (2011) *J. Mater. Chem.*, **21** (35), 13464–13469.
29 Li, F., Vipulanandan, C., and Mohanty, K.K. (2003) *Colloids Surf. Physicochem. Eng. Asp.*, **223** (1), 103–112.
30 Carpenter, E., Sims, J., Wienmann, J. *et al.* (2000) *J. Appl. Phys.*, **87** (9), 5615–5617.
31 Guo, L., Huang, Q., Li, X.-Y. *et al.* (2001) *Phys. Chem. Chem. Phys.*, **3** (9), 1661–1665.
32 Chen, J., Sorensen, C., Klabunde, K. *et al.* (1995) *Phys. Rev. B*, **51** (17), 11527.
33 Lin, X., Sorensen, C., Klabunde, K. *et al.* (1998) *Langmuir*, **14** (25), 7140–7146.
34 Lin, X., Sorensen, C., Klabunde, K. *et al.* (1999) *J. Mater. Res.*, **14** (4), 1542–1547.
35 Petit, C., Taleb, A., and Pileni., M. (1999) *J. Phys. Chem. B*, **103** (11), 1805–1810.
36 Sun, S. and Murray, C. (1999) *J. Appl. Phys.*, **85** (8), 4325–4330.
37 Puntes, V.F., Zanchet, D., Erdonmez, C.K. *et al.* (2002) *J. Am. Chem. Soc.*, **124** (43), 12874–12880.
38 Dumestre, F., Chaudret, B., Amiens, C. *et al.* (2003) *Angew. Chem., Int. Ed.*, **42** (42), 5213–5216.
39 Dumestre, F., Chaudret, B., Amiens, C. *et al.* (2002) *Angew. Chem.*, **114** (22), 4462–4465.
40 Puntes, V.F., Krishnan, K.M., and Alivisatos, A.P. (2001) *Supramol. Sci.*, **291** (5511), 2115–2117.
41 Peng, Z.A. and Peng, X. (2001) *J. Am. Chem. Soc.*, **123** (7), 1389–1395.
42 Petroski, J.M., Wang, Z.L., Green, T.C. *et al.* (1998) *J. Phys. Chem. B*, **102** (18), 3316–3320.
43 Bradley, J.S., Tesche, B., Busser, W. *et al.* (2000) *J. Am. Chem. Soc.*, **122** (19), 4631–4636.
44 Hou, Y., Kondoh, H., Ohta, T. *et al.* (2005) *Appl. Surf. Sci.*, **241** (1), 218–222.
45 Osuna, J., Caro, D.de., Amiens, C. *et al.* (1996) *J. Phys. Chem.*, **100** (35), 14571–14574.
46 Pick, Š. and Dreyssé, H. (2000) *Surf. Sci.*, **460** (1), 153–161.
47 Cordente, N., Respaud, M., Senocq, F. *et al.* (2001) *Nano Lett.*, **1** (10), 565–568.
48 Sun., S. (2006) *Adv. Mater.*, **18** (4), 393–403.

49 Gutfleisch, O., Lyubina, J., Müller, K.H. *et al.* (2005) *Adv. Eng. Mater.*, **7** (4), 208–212.
50 Burkert, T., Eriksson, O., Simak, S.I. *et al.* (2005) *Phys. Rev. B*, **71** (13), 134411.
51 Brown, G., Kraczek, B., Janotti, A. *et al.* (2003) *Phys. Rev. B*, **68** (5), 052405.
52 Staunton, J., Ostanin, S., Razee, S. *et al.* (2004) *Phys. Rev. Lett.*, **93** (25), 257204.
53 Weller, D., Moser, A., Folks, L. *et al.* (2000) *IEEE Trans. Magn.*, **36** (1), 10–15.
54 Luo, C. and Sellmyer, D.J. (1995) *IEEE Trans. Magn.*, **36** (1), 2764–2766.
55 Hsu, Y.-N., Jeong, S., Laughlin, D.E. *et al.* (2001) *J. Appl. Phys.*, **89** (11), 7068–7070.
56 Kitakami, O., Shimada, Y., Oikawa, K. *et al.* (2001) *Appl. Phys. Lett.*, **78** (8), 1104–1106.
57 Maeda, T., Kai, T., Kikitsu, A. *et al.* (2002) *Appl. Phys. Lett.*, **80** (12), 2147–2149.
58 Mukherjee, P., Manchanda, P., Kumar, P. *et al.* (2014) *ACS Nano*, **8** (8), 8113–8120.
59 Langlois, C., Benzo, P., Arenal, R. *et al.* (2015) *Nano Lett.*, **15** (8), 5075–5080.
60 Weller, D., Brändle, H., Gorman, G. *et al.* (1992) *Appl. Phys. Lett.*, **61** (22), 2726–2728.
61 Sanchez, J., Moran-Lopez, J., Leroux, C. *et al.* (1989) *J. Phys. Condens. Mater.*, **1** (2), 491.
62 Yu, Y., Yang, W., Sun, X. *et al.* (2014) *Nano Lett.*, **14** (5), 2778–2782.
63 Shevchenko, E.V., Talapin, D.V., Rogach, A.L. *et al.* (2002) *J. Am. Chem. Soc.*, **124** (38), 11480–11485.
64 Shevchenko, E.V., Talapin, D.V., Schnablegger, H. *et al.* (2003) *J. Am. Chem. Soc.*, **125** (30), 9090–9101.
65 Takahashi, Y., Koyama, T., Ohnuma, M. *et al.* (2004) *J. Appl. Phys.*, **95** (5), 2690–2696.
66 Gruner, M.E., Rollmann, G., Entel, P. *et al.* (2008) *Phys. Rev. Lett.*, **100** (8), 087203.
67 Stahl, B., Ellrich, J., Theissmann, R. *et al.* (2003) *Phys. Rev. B*, **67** (1), 014422.
68 Wiedwald, U., Klimmer, A., Kern, B. *et al.* (2007) *Appl. Phys. Lett.*, **90** (6), 62508–62508.
69 Antoniak, C., Lindner, J., Spasova, M. *et al.* (2006) *Phys. Rev. Lett.*, **97** (11), 117201.
70 Himpsel, F., Ortega, J., Mankey, G. *et al.* (1998) *Adv. Phys.*, **47** (4), 511–597.
71 Sato, K., Bian, B., and Hirotsu., Y. (2002) *J. Appl. Phys.*, **91** (10), 8516–8518.
72 Sato, K. and Hirotsu, Y. (2004) *J. Magn. Magn. Mater.*, **272**, 1497–1499.
73 Yasuda, H. and Mori, H. (1996) *Z. Phys. D Atoms, Mol. Clusters*, **37** (2), 181–186.
74 Miyazaki, T., Kitakami, O., Okamoto, S. *et al.* (2005) *Phys. Rev. B*, **72** (14), 144419.
75 Takahashi, Y., Ohkubo, T., Ohnuma, M. *et al.* (2003) *J. Appl. Phys.*, **93** (10), 7166–7168.
76 Sato, K., Hirotsu, Y., Mori, H. *et al.* (2005) *J. Appl. Phys.*, **98** (2), 24308
77 Yang, B., Asta, M., Mryasov, O. *et al.* (2006) *Acta Mater.*, **54** (16), 4201–4211.
78 Chepulskii, R. and Butler, W. (2005) *Phys. Rev. B*, **72** (13), 134205.
79 Müller, M. and Albe, K. (2005) *Phys. Rev. B*, **72** (9), 094203.

80 Moskovkin, P., Pisov, S., Hou, M. *et al.* (2007) *Eur. Phys. J. D*, **43** (1–3), 27–32.
81 Moskovkin, P. and Hou, M. (2007) *J. Alloys Compd.*, **434**, 550–554.
82 Alloyeau, D., Ricolleau, C., Mottet, C. *et al.* (2009) *Nat. Mater.*, **8** (12), 940–946.
83 Abrikosov, I.A., Kissavos, A.E., Liot, F. *et al.* (2007) *Phys. Rev. B*, **76** (1), 014434.
84 van Schilfgaarde, M., Abrikosov, I., and Johansson, B. (1999) *Nature*, **400** (6739), 46–49.
85 Dang, M.-Z. and Rancourt, D. (1996) *Phys. Rev. B*, **53** (5), 2291.
86 Rancourt, D. and Scorzelli, R. (1995) *J. Magn. Magn. Mater.*, **150** (1), 30–36.
87 Reuter, K., Williams, D.B., and Goldstein., J. (1989) *Metall. Trans. A*, **20** (4), 719–725.
88 Rao, B., de Debiaggi, S.R., and Jen, P. (2001) *Phys. Rev. B*, **64** (2), 024418.
89 Xu, M., Zhong, W., Qi, X. *et al.* (2010) *J. Alloys Compd.*, **495** (1), 200–204.
90 Moustafa, S. and Daoush, W. (2007) *J. Mater. Process. Technol.*, **181** (1), 59–63.
91 Zhang, X., Zhang, H., Wu, T. *et al.* (2013) *J. Magn. Magn. Mater.*, **331**, 162–167.
92 Wang, H., Li, J., Kou, X. *et al.* (2008) *J. Cryst. Growth*, **310** (12), 3072–3076.
93 Wei, X.-W., Zhu, G.-X., Xia, C.-J. *et al.* (2006) *Nanotechnology*, **17** (17), 4307.
94 Yu, R., Basu, S., Zhang, Y. *et al.* (1999) *J. Appl. Phys.*, **85**, 6034–6036.
95 Li, L. (1996) *J. Appl. Phys.*, **79** (8), 4578–4580.
96 Paulus, P., Luis, F., Kröll, M. *et al.* (2001) *J. Magn. Magn. Mater.*, **224** (2), 180–196.
97 Qin, D., Cao, L., Sun, Q. *et al.* (2002) *Chem. Phys. Lett.*, **358** (5), 484–488.
98 Burkert, T., Nordström, L., Eriksson, O. *et al.* (2004) *Phys. Rev. Lett.*, **93** (2), 027203.
99 Collier, K., Jones, N., Miller, K. *et al.* (2009) *J. Appl. Phys.*, **105** (7), 07A328.
100 Hergt, R., Dutz, S., Müller, R. *et al.* (2006) *J. Phys. Condens. Matter*, **18** (38), S2919.
101 Hergt, R., Andra, W., d'Ambly, C.G. *et al.* (1998) *IEEE Trans. Magn.*, **34** (5), 3745–3754.
102 Hergt, R. and Dutz, S. (2007) *J. Magn. Magn. Mater.*, **311** (1), 187–192.
103 Alonso, J., Khurshid, H., Sankar, V. *et al.* (2015) *J. Appl. Phys.*, **117** (17), 17D113.
104 Seo, W.S., Lee, J.H., Sun, X. *et al.* (2006) *Nat. Mater*, **5** (12), 971–976.
105 Ung, D., Viau, G., Ricolleau, C. *et al.* (2005) *Adv. Mater.*, **17** (3), 338–344.
106 Vivas, L., Vazquez, M., Escrig, J. *et al.* (2012) *Phy. Rev. B*, **85** (3), 035439.
107 Mayergoyz, I. (1985) *J. Appl. Phys.*, **57** (8), 3803–3805.
108 Didziulis, S.V., Butcher, K.D., and Perry., S.S. (2003) *Inorg. Chem.*, **42** (24), 7766–7781.
109 Neuhaus, A., Veldkamp, A., and Frenking., G. (1994) *Inorg. Chem.*, **33** (23), 5278–5286.
110 Hugosson, H.W., Eriksson, O., Jansson, U. *et al.* (2004) *Surf. Sci.*, **557** (1), 243–254.
111 Costales, A., Blanco, M.A., Pendás, Á.M. *et al.* (2002) *J. Am. Chem. Soc.*, **124** (15), 4116–4123.
112 Jansen, S.A. and Hoffmann., R. (1988) *Surf. Sci.*, **197** (3), 474–508.
113 Hwu, H.H. and Chen, J.G. (2005) *Chem. Rev.*, **105** (1), 185–212.

114 Levin, A., Meyer, D., Reibold, M. *et al.* (2005) *Cryst. Res. Technol.*, **40** (9), 905–916.
115 Arbuznikov, A.V., Hendrickx, M., and Vanquickenborne, L.G. (1999) *Chem. Phys. Lett.*, **310** (5–6), 515–522.
116 Cao, Z. (1996) *J. Mol. Struct. Theochem.*, **365** (2–3), 211–214.
117 Wang, L.-S. (1996) *Surf. Rev. Lett.*, **03** (1), 423–427.
118 Gutsev, G.L. and Bauschlicher, C.W., Jr., (2003) *Chem. Phys.*, **291** (1), 27–40.
119 Tzeli, D. and Mavridis, A. (2005) *J. Phys. Chem. A*, **109** (41), 9249–9258.
120 Noya, E.G., Longo, R.C., and Gallego., L.J. (2003) *J. Chem. Phys.*, **119** (21), 11130–11134.
121 Nash, B.K., Rao, B., and Jen, P. (1996) *J. Chem. Phys.*, **105** (24), 11020–11023.
122 Fang, C., Van Huis, M., and Zandbergen., H. (2009) *Phy. Rev. B*, **80** (22), 224108.
123 Yang, Z., Zhao, T., Huang, X. *et al.* (2017) *Chem. Sci.*, **8** (1), 473–481.
124 Carroll, K.J., Huba, Z.J., Spurgeon, S.R. *et al.* (2012) *Appl. Phys. Lett.*, **101** (1), 012409.
125 Zhang, Y., Chaubey, G.S., Rong, C. *et al.* (2011) *J. Magn. Magn. Mater.*, **323** (11), 1495–1500.
126 Suzuki, K., Morita, H., Kaneko, T. *et al.* (1993) *J. Alloys Compd.*, **201** (1–2), 11–16.
127 Sakuma, A. (1991) *J. Magn. Magn. Mater.*, **102** (1–2), 127–134.
128 Nagakura, S. (1958) *J. Phys. Soc. Jpn.*, **13** (9), 1005–1014.
129 Shein, I., Medvedeva, N., and Ivanovskii, A. (2006) *Phys. B*, **371** (1), 126–132.
130 Neklyudov, I. and Morozov, A. (2004) *Phys. B*, **350** (4), 325–337.
131 Hwang, J.Y., Singh, A.R., Chaudhari, M. *et al.* (2010) *J. Phys. Chem. C*, **114** (23), 10424–10429.
132 Choi, J. and Gillan., E.G. (2009) *Inorg. Chem.*, **48** (10), 4470–4477.
133 Ghosh, B., Dutta, H., and Pradhan, S. (2009) *J. Alloys Compd.*, **479** (1), 193–200.
134 Yue, L., Sabiryanov, R., Kirkpatrick, E. *et al.* (2000) *Phy. Rev. B*, **62** (13), 8969.
135 Fang, C., Sluiter, M., van Huis, M. *et al.* (2012) *Phy. Rev. B*, **86** (13), 134114.
136 Cornell, R.M. and Schwertmann, U. (2003) *The Iron Oxides: Structure, Properties, Reactions, Occurrences and Uses*, John Wiley & Sons, Inc., New York.
137 Yang, C., Wu, J., and Hou, Y. (2011) *Chem. Commun.*, **47** (18), 5130–5141.
138 Ho, D., Sun, X., and Sun, S. (2011) *Acc. Chem. Res.*, **44** (10), 875–882.
139 Park, J., An, K., Hwang, Y. *et al.* (2004) *Nat. Mater.*, **3** (12), 891–895.
140 Hou, Y., Xu, Z., and Sun, S. (2007) *Angew. Chem.*, **119** (33), 6445–6448.
141 Agilandeswari, K. and Rubankumar, A. (2016) *Inorg. Nano-Metal Chem..* **46** (4), 502–506.
142 Devan, R.S., Patil, R.A., Lin, J.H. *et al.* (2012) *Adv. Funct. Mater.*, **22** (16), 3326–3370.
143 Song, L.X., Yang, Z.K., Teng, Y. *et al.* (2013) *J. Mater. Chem. A*, **1** (31), 8731–8736.
144 Faraji, S. and Ani, F.N. (2014) *J. Power Sources*, **263**, 338–360.
145 Ma, R., Bando, Y., Zhang, L. *et al.* (2004) *Adv. Mater.*, **16** (11), 918–922.
146 Vargas, O., Caballero, A., Hernán, L. *et al.* (2011) *J. Power Sources*, **196** (6), 3350–3354.

147 Li, Y., Wang, J., Zhang, Y. *et al.* (2012) *J. Colloid Interface Sci.*, **369** (1), 123–128.
148 Djerdj, I., Arčon, D., Jagličic, Z. *et al.* (2007) *J. Phys. Chem. C*, **111** (9), 3614–3623.
149 Kirchmayr, H. (1996) *J. Phys. D Appl. Phys.*, **29** (11), 2763.
150 Gutfleisch, O., Willard, M.A., Brück, E. *et al.* (2011) *Adv. Mater.*, **23** (7), 821–842.
151 Hou, Y., Xu, Z., Peng, S. *et al.* (2007) *Adv. Mater.*, **19** (20), 3349–3352.
152 Xue, Z., Liu, L., Liu, Z. *et al.* (2016) *Scr. Mater.*, **113**, 226–230.
153 Chaban, N., Kuz'ma, Y.B., Bilonizhko, N. *et al.* (1979) *Dopovidi Akad. Nauk Ukr. RSR, Ser. A*, **10**, 873–875.
154 McCallum, R., Lewis, L., Skomski, R. *et al.* (2014) *Annu. Rev. Mater. Res.*, **44**, 451–477.
155 Coey, J. and Sun, H. (1990) *J. Magn. Magn. Mater.*, **87** (3), L251–L254.
156 Stöhr, J. (1999) *J. Magn. Magn. Mater.*, **200** (1), 470–497.
157 Funk, T., Deb, A., George, S.J. *et al.* (2005) *Coord. Chem. Rev.*, **249** (1), 3–30.
158 Carra, P., Thole, B., Altarelli, M. *et al.* (1993) *Phys. Rev. Lett.*, **70** (5), 694.
159 Stöhr, J., Wu, Y., Hermsmeier, B. *et al.* (1993) *Science*, **259**, 658
160 Stöhr, J., Padmore, H., Anders, S. *et al.* (1998) *Surf. Rev. Lett.*, **5** (06), 1297–1308.
161 Kang, J.-S., Kim, G., Lee, H. *et al.* (2008) *Phy. Rev. B*, **77** (3), 035121.
162 Schofield, M., Beleggia, M., Zhu, Y. *et al.* (2008) *Ultramicroscopy*, **108** (7), 625–634.
163 Petford-Long, A. and Chapman, J. (2005) *Magnetic Microscopy of Nanostructures*, Springer.
164 Reimer, L. (2013) *Transmission Electron Microscopy: Physics of Image Formation and Microanalysis*, Springer.
165 McFadyen, I. and Chapman, J. (1992) *EMSA Bull.*, **22**, 64–75.
166 Doole, R., Petford-Long, A., and Jakubovics, J. (1993) *Rev. Sci. Instrum.*, **64** (4), 1038–1043.
167 Tsuno, K. and Inoue, M. (1984) *Optik*, **67** (4), 363–376.
168 Tsuno, K. and Taoka, T. (1983) *Jpn. J. Appl. Phys.*, **22** (6R), 1041.
169 Tian, Y., Liu, Z., Xu, H. *et al.* (2015) *IEEE Trans. Magn.*, **51** (11), 1–4.
170 Seki, S., Yu, X., Ishiwata, S. *et al.* (2012) *Supramol. Sci.*, **336** (6078), 198–201.
171 Rößler, U., Bogdanov, A., and Pfleiderer, C. (2006) *Nature*, **442** (7104), 797–801.
172 Binz, B., Vishwanath, A., and Aji, V. (2006) *Phys. Rev. Lett.*, **96** (20), 207202.
173 Mühlbauer, S., Binz, B., Jonietz, F. *et al.* (2009) *Supramol. Sci.*, **323** (5916), 915–919.
174 Yu, X., Onose, Y., Kanazawa, N. *et al.* (2010) *Nature*, **465** (7300), 901–904.
175 Yu, X., Kanazawa, N., Onose, Y. *et al.* (2011) *Nat. Mater.*, **10** (2), 106–109.
176 Tonomura, A., Yu, X., Yanagisawa, K. *et al.* (2012) *Nano Lett.*, **12** (3), 1673–1677.
177 Kanazawa, N., Kim, J.-H., Inosov, D. *et al.* (2012) *Phy. Rev. B*, **86** (13), 134425.
178 Shibata, K., Yu, X., Hara, T. *et al.* (2013) *Nat. Nanotechnol.*, **8** (10), 723–728.
179 Greneche, J.-M. (2013) *Mössbauer Spectroscopy*, Springer.
180 Gütlich, P. and Garcia, Y. (2013) *Mössbauer Spectroscopy*, Springer.
181 Mössbauer, R.L. (1958) *Z. Phys.*, **151** (2), 124–143.

182 Mössbauer, R.L. (2000) *Hyperfine Interact.*, **126** (1), 1–12.
183 Nasu, S. (2013) *Mössbauer Spectroscopy*, Springer.
184 Wertheim, G.K. (2013) *Mössbauer Effect: Principles and Applications*, Academic Press.
185 Kistner, O. and Sunyar, A. (1960) *Phys. Rev. Lett.*, **4** (8), 412.
186 Verwey, E. (1939) *Nature*, **144** (3642), 327–328.
187 Verwey, E., Haayman, P., and Romeijn, F. (1947) *J. Chem. Phys.*, **15** (4), 181–187.
188 Verwey, E. and Heilmann, E. (1947) *J. Chem. Phys.*, **15** (4), 174–180.
189 Leonov, I. and Yaresko, A. (2007) *J. Phys. Condens. Matter*, **19** (2), 021001.
190 Koningsberger, D. and Prins, R. (1988) X-ray absorption: principles, applications, techniques of EXAFS, SEXAFS, and XANES, Wiley-VCH Verlag GmbH.
191 Schütz, G., Frahm, R., Mautner, P. *et al.* (1989) *Phys. Rev. Lett.*, **62** (22), 2620.
192 Schütz, G., Knülle, M., Wienke, R. *et al.* (1988) *Z. Phys. B Condens. Matter*, **73** (1), 67–75.
193 Schütz, G., Wagner, W., Wilhelm, W. *et al.* (1987) *Phys. Rev. Lett.*, **58** (7), 737.
194 Schütz, G., Wienke, R., Wilhelm, W. *et al.* (1989) *Z. Phys. B Condens. Matter*, **75** (4), 495–500.
195 Ebert, H., Popescu, V., and Ahlers., D. (1999) *Phy. Rev. B*, **60** (10), 7156.
196 Martin, Y. and Wickramasinghe, H.K. (1987) *Appl. Phys. Lett.*, **50** (20), 1455–1457.
197 Rugar, D., Mamin, H., Guethner, P. *et al.* (1990) *J. Appl. Phys.*, **68** (3), 1169–1183.
198 Hartmann, U. (1999) *Annu. Rev. Mater. Sci.*, **29** (1), 53–87.
199 Göddenhenrich, T., Hartmann, U., Anders, M. *et al.* (1870) *J. R. Microsc. Soc.*, **3** (3), 527–536.
200 Göddenhenrich, T., Lemke, H., Mück, M. *et al.* (1990) *Appl. Phys. Lett.*, **57** (24), 2612–2614.
201 Moser, A., Hug, H., Parashikov, I. *et al.* (1995) *Phys. Rev. Lett.*, **74** (10), 1847.
202 Hoffmann, B., Houbertz, R., and Hartmann., U. (1998) *Appl. Phys. A Mater. Sci. Process.*, **66**, S409–S413.
203 Wang, T., Wang, Y., Fu, Y. *et al.* (2009) *Nanotechnology*, **20** (10), 105707.
204 Bramwell, S.T. and Gingras, M.J. (2001) *Supramol. Sci.*, **294** (5546), 1495–1501.
205 Ramirez, A.P., Hayashi, A., Cava, R. *et al.* (1999) *Nature*, **399** (6734), 333–335.
206 Sherrington, D. and Kirkpatrick, S. (1975) *Phys. Rev. Lett.*, **35** (26), 1792.
207 Ladak, S., Read, D., Perkins, G. *et al.* (2010) *Nat. Phys.*, **6** (5), 359–363.
208 Fagaly, R. (2006) *Rev. Sci. Instrum.*, **77** (10), 101101.
209 Lenz, J. and Edelstein, A.S. (2006) *IEEE Sens. J.*, **6** (3), 631–649.
210 Lenz, J.E. (1990) *Proc. IEEE*, **78** (6), 973–989.
211 Webb, R.A. (1977) *Rev. Sci. Instrum.*, **48** (12), 1585–1594.
212 Klemme, B.J., Adriaans, M.J., Day, P.K. *et al.* (1999) *J. Low Temp. Phys.*, **116** (1), 133–146.
213 Solomonson, N., Hamilton, W.O., Johnson, W. *et al.* (1994) *Rev. Sci. Instrum.*, **65** (1), 174–181.